High resolution digital transmission microscopy : a Fourier holography approach

Gustafsson, Mats; Sebesta, Mikael; Bengtsson, Bengt A; Pettersson, Sven-Göran; Egelberg, Peter; Lenart, Thomas

2002

CODEN:LUTEDX/(TEAT-7106)/1-11/(2002)

High resolution digital transmission microscopy—a Fourier holography approach

Mats Gustafsson, Mikael Sebesta, Bengt Bengtsson, Sven-Göran Pettersson, Peter Egelberg, and Thomas Lenart

Department of Electroscience
Electromagnetic Theory
Lund Institute of Technology
Sweden

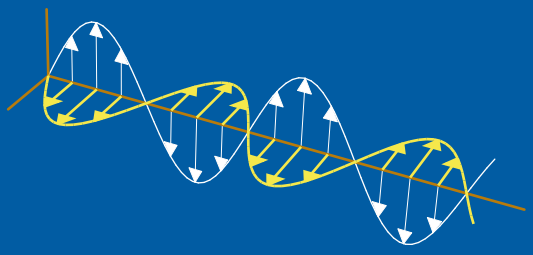

Mats Gustafsson, Bengt Bengtsson, and Thomas Lenart

Department of Electroscience
Lund Institute of Technology
P.O. Box 118
SE-221 00 Lund
Sweden

Sven-Göran Pettersson

Atomic Physics
Lund Institute of Technology
P.O. Box 118
SE-221 00 Lund
Sweden

Mikael Sebesta and Peter Egelberg

Neural AB
SE-224 75 Lund
Sweden

Editor: Gerhard Kristensson

Abstract

A spherical reference field is used to construct a digital holography system with a demonstrated resolution down to 228 line pairs per mm. The reference field origin from a GRIN lens placed 1 mm from the illuminated object. This allows the use of a standard sensor to record the hologram with the required numerical aperture. The image is determined by evaluation of the Rayleigh-Sommerfeld diffraction integral that relates the object field in the image plane to the object field in the sensor plane. Experimental results are given for two charge couple device sensors and one complementary metal-oxide-semiconductor active pixel sensor.

1 Introduction

Digital holography has several features that makes it an interesting alternative to conventional microscopy. These features include an improved depth focus, possibility to generate three-dimensional images, and phase contrast images [3, 4, 7, 12, 14–17]. The experimental setup in digital holography is a trade off between resolution, computational complexity, and experimental simplicity. Two popular versions are the digital Fresnel holography and the digital inline holography. The digital Fresnel holography uses quasi parallel beams [11]. In digital inline holography, a point source is used to illuminate the object and at the same time act as the reference wave. This setup works very well for highly transparent objects, *i.e.*, low contrast objects, and it has both a high lateral and a high depth resolution [12, 17]. Here, digital Fourier holography is considered where the reference field origin from a point source located in the object plane close to the illuminated object [6, 8, 13, 15]. Both low and high contrast objects can be imaged with this setup. It offers a high transverse resolution, a high depth of field, and a typical microscope depth resolution. The transverse resolution is experimentally demonstrated down to 228 line pairs per mm.

A high resolution requires the recording of the hologram in a large numerical aperture (NA) of the object. For a digital sensor, the numerical aperture can either be increased by a shortened object-sensor distance or by an enlarged sensor. The object-sensor distance is limited by the elementary pixel distance of the sensor from the requirement to sample the hologram at or above the Nyquist limit [10, 11]. The spatial frequencies of the hologram can be minimized by the use of quasi parallel beams, a short object-reference distance, or a small object, as used in Fresnel holography, Fourier holography, and inline holography, respectively. In the present Fourier holography setup, a GRIN lens placed 1 mm from the illuminated object is used to create a spherical reference field. This gives approximately the same curvature of the reference field and the object field. And, hence, the possibility to record the hologram with a standard sensor at an object-sensor distance of $4 - 5$ cm and a numerical aperture of 0.17.

The image reconstruction is performed by evaluation of the Rayleigh-Sommerfeld diffraction integral that relates the object field in the image plane to the object

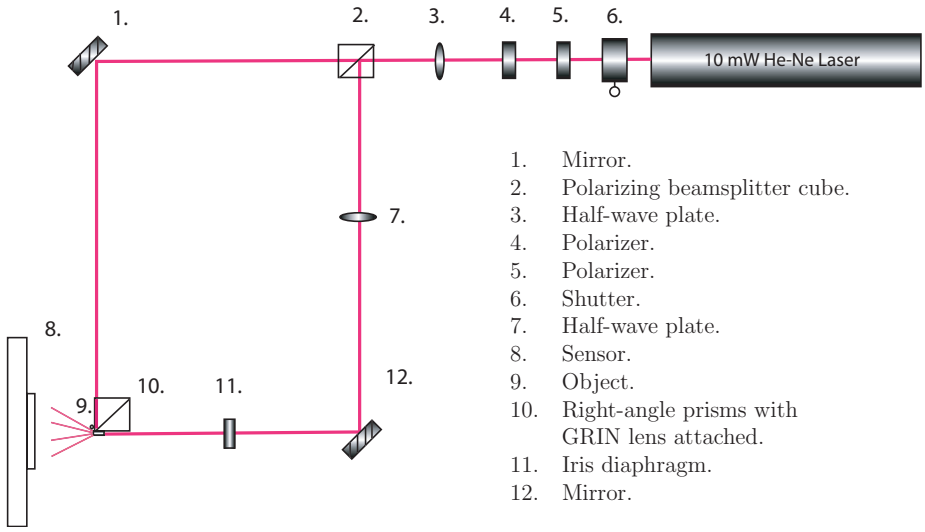

Figure 1: The experimental Fourier holography setup.

field in the sensor plane [2, 10]. Due to the large numerical aperture and the large objects neither the Fresnel nor the Fraunhofer approximation are applicable. Instead the convolution structure of the integral is used to accelerate the evaluations with fast Fourier transformations (FFT) [5]. The FFT structure is also favorable for a hardware implementation of the algorithm [9].

In this paper, digital Fourier holography with three different sensors are compared. The two first sensors, Kodak KAF3200E and Mintron MTV-1802CB, are charge coupled device (CCD) sensors whereas the third sensor, STMicroelectronics VV5410, is a complementary metal-oxide-semiconductor active pixel (CMOS) sensor. The sensor have different elementary pixel distances, number of pixels, and dynamics. The highest resolution is achieved with the Kodak KAF3200E sensor that both has the smallest elementary pixels, large number of pixels, and largest dynamics.

The organization of the paper is as follows. In Section 2, the experimental setup is described. The inversion algorithm is discussed in Section 3. Experimental results are presented in Section 4. The results are discussed in Section 5.

2 Experimental setup

One of the aims of this work is to construct a simple yet flexible lens less holographic microscope setup. This is accomplished by the simple arrangement in Figure 1, see also Figure 2. The light source in the setup is a JDS Uniphase 10 mW polarized He-Ne laser with a wavelength of $\lambda = 633\,\text{nm}$. The two polarizers enable variation of the intensity of the beam which is then divided into a reference beam and an object beam by the polarizing beam splitter cube. Together with two half-wave plates, the intensity in the reference beam and the object beam can be controlled and at the same time keep the polarization of the fields linear.

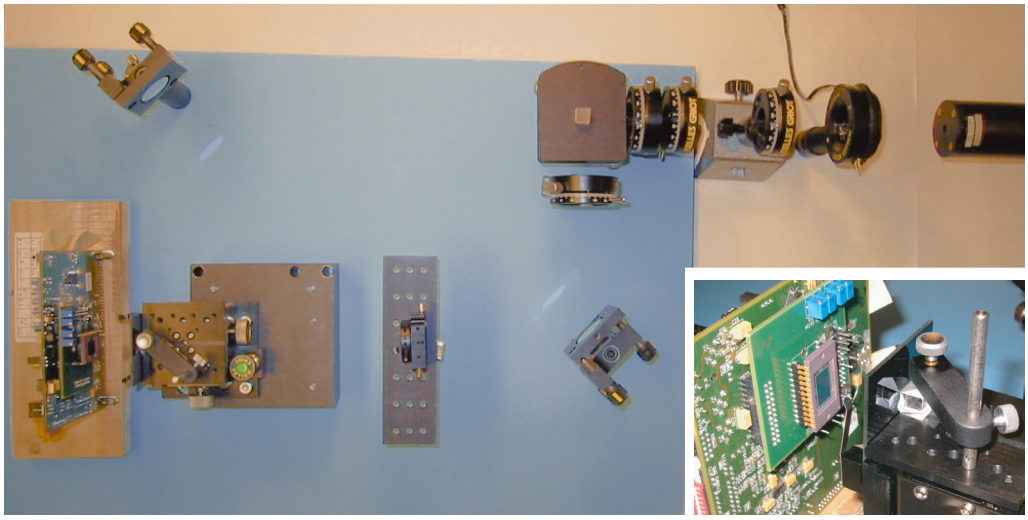

Figure 2: Photo of the setup with an enlargement of the right-angle prism and its attached GRIND lens. The components are described in Figure 1.

The experimental Fourier holography setup implies a spherical reference point source close to the illuminated object. This gives approximately the same curvature of the reference field and the object field and hence low spatial frequencies of the hologram. To achieve a large numerical aperture of the reference field and keep the point source close to the object a 0.25 pitch GRIN lens is used to widen the reference beam. The GRIN lens has a numerical aperture of 0.37, a diameter of 1.0 mm, and is placed on the side of a right angle prism which directs the object beam on to the object. The arrangement with the GRIN lens gives a minimum distance between the object and the point source of about 0.5 mm and at the same time the possibility to vary the intensity of both the point source and the object illumination respectively.

A USAF chromium negative test target is used as object with a maximum resolution of 228 line pairs/mm. The object beam illuminates the 5th to the 7th series of the test target while the reference point source is placed in the quadratic shape of the 3rd series. This gives a distance between the point source and the illuminated series of about 1.0 mm. When placing the reference source behind the test target internal interference in the test target causes disturbances in the reference field. Fortunately this does not deteriorate the reconstructed holograms visibly.

Three different images are taken to reconstruct one holographic image. Simply by blocking either the reference beam or the object beam images of the reference, the object, and the hologram are gathered. The sensors described in Table 1 were used to collect the images. The numerical aperture (NA) of each sensor is estimated as

$$\mathrm{NA} = \frac{N_{\mathrm{Sx}} \Delta x/2}{\sqrt{\left(N_{\mathrm{Sx}} \Delta x/2\right)^2 + L^2}} = \frac{N_{\mathrm{Sx}}}{\sqrt{N_{\mathrm{Sx}}^2 + \left(2N_{\mathrm{spw}} d/\lambda\right)^2}}, \tag{2.1}$$

where N_{Sx}, L, d, and N_{spw} are the number of pixels, the minimal object-sensor distance, the maximal object-reference distance, and the required number of pixels per fringe, respectively. The values on NA in Table 1 are determined for the object-

sensor	N_{Sx}	N_{Sy}	Δx	Δy	bits	NA
Kodak KAF3200E	2184	1472	$6.8\,\mu$m	$6.8\,\mu$m	12	0.33
Mintron MTV-1802CB	795	596	$8.05\,\mu$m	$8.05\,\mu$m	8	0.12
STMicroelectronics VV5410	350	296	$7.5\,\mu$m	$6.9\,\mu$m	8	0.055

Table 1: Sensor specification. N_{Sx}, N_{Sy}, Δx, and Δy are the number of pixels and pixel sampling in the x, y directions, respectively. NA is the maximal numerical aperture (2.1) for the sensor with a object-reference distance of 1 mm and a sample of 2 pixels per fringe, *i.e.*, the Nyquist limit [10].

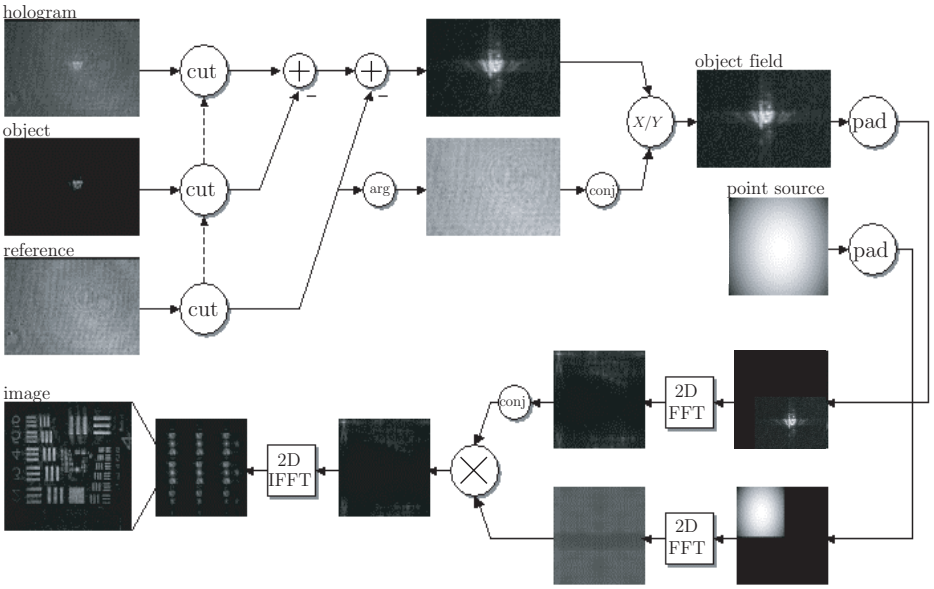

Figure 3: Flow chart of the imaging algorithm. The recorded hologram, object, and reference images are first used to construct an approximate object field (3.1) as depicted in the upper row. The second row illustrates the Fast Fourier Transform (FFT) techniques that are used to evaluate the convolutional integral (3.3).

reference distance $d = 1\,$mm and the sampling $N_{\mathrm{spw}} = 2$ pixels per fringe. Observe that this is a theoretical NA in practice an oversampling is required [10]. For the Kodak KAF3200E sensor, a sampling with 4.1 pixels per fringe was shown to be practical. This corresponds to a NA of 0.17.

3 Inversion algorithm

In the experimental setup it is not possible to measure the object field E_{o} directly. Instead an approximation of the object field is determined from the interference pattern between the object field and the reference field E_{r}, *i.e.*, a sampled version of the interference pattern $|E_{\mathrm{o}} + E_{\mathrm{r}}|^2$ is measured by the sensor. With additional

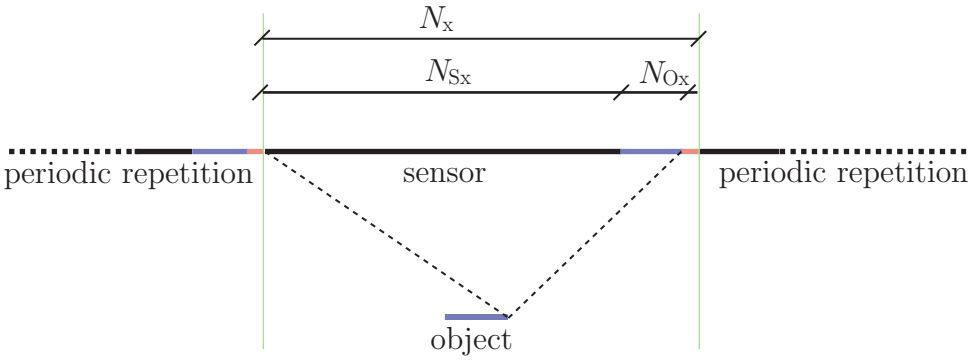

Figure 4: Geometry for the inversion. The FFT is performed on an $N_x \times N_y$ array, where N_x and N_x are composed by small primes. To avoid the aliasing effects, the length N_x has to be longer then the sum of the sensor length N_{Sx} and the object length N_{Ox}, and similarly for the y direction.

measurements of $|E_o|^2$ and $|E_r|^2$ the object field is approximated with $\widetilde{E}_o$ as

$$\widetilde{E}_o = E_o E_r^*/\widetilde{E}_r^* + E_o^* E_r/\widetilde{E}_r^* = (|E_o + E_r|^2 - |E_o|^2 - |E_r|^2)/\widetilde{E}_r^* \tag{3.1}$$

where $\widetilde{E}_r$ is the the approximate reference field, see also Figure 3. It is assumed that the reference field is a spherical wave, *i.e.*, $\widetilde{E}_r = |E_r|e^{-ikr}$ where $k = 2\pi/\lambda$ is the wave number. With an accurate reference field $\widetilde{E}_r = E_r$, the error term $E_o^* E_r/\widetilde{E}_r^*$ produces a conjugate image [2].

The approximate object field is used to determine an image of the object. The image is identified with the equivalent field distribution E_i that induces the object field on the sensor. The image field in the image plane is related to the object field on the sensor by the Rayleigh-Sommerfeld diffraction integral [2, 10], *i.e.*,

$$\widetilde{E}_o(\xi, \eta) = \iint G_d(x - \xi, y - \eta, z) E_i(x, y, z)\, dx\, dy, \tag{3.2}$$

where G_d is the Green function that relates the E-field in the image plane to the E-field in the sensor plane. Inversion of this integral gives the image field and hence also the image. To invert (3.2), a back propagation is used, *i.e.*, the wave field is retrofocused towards its source distribution. The back propagated object field is given by the Rayleigh-Sommerfeld diffraction integral that relates the image field in the image plane to the object field in the sensor plane

$$E_i(x, y, z) = 2 \iint \frac{\partial G}{\partial z}(x - \xi, y - \eta, z) \widetilde{E}_o^*(\xi, \eta)\, d\xi\, d\eta, \tag{3.3}$$

where the Green function is $G(\boldsymbol{r}) = e^{-ik|\boldsymbol{r}|}/(4\pi|\boldsymbol{r}|)$. This integral is discretized on the equidistant grid $(\Delta x, \Delta y)$ generated by the sensor sampling to produce a discrete convolution that can be evaluated with the FFT [5]. Additional refinement of the object is given by a shifting the coordinates a fraction of the sampling length. The first evaluation requires three FFTs whereas each additional evaluation only requires

two FFTs. Due to the periodic structure of the FFT it is not possible to perform the FFT on the sensor array without zero padding. Fortunately, it is enough to perform the FFT on an array with dimensions given by the sum of the sensor lengths and the object lengths, see Figure 4.

The present algorithm is chosen because of its simplicity, accuracy, and generality. The algorithm is accurate since no asymptotic approximations of (3.3) are performed, *i.e.*, the integral can be evaluated to an arbitrary precision. It is also possible to generalize the algorithm to more complex geometries, such as the case of a glass plate between the object and the sensor. This offers the possibility to compensate for this kind of disturbances in the inversion algorithm. The drawback of the algorithm is that several FFTs has to be performed to achieve a sub-pixel resolution. This can be compared with the Fraunhofer approximation that gives the Kirchhoff-Helmholtz integral [17] and hence also a refined sampling in the image plane. However, due to the large objects used here, the Fraunhofer approximation is not applicable.

4 Experimental results

The microscope set-up, previously described in Section 2, was tested to evaluate its capacity in resolving a USAF test target. The resolving power arise from the numerical aperture. For comparison three different cameras were tested as described in Table 1. As one can conclude from Figure 5 the best resolution was achieved with the Kodak KAF3200E CCD camera. The physical resolution limit of an optical system is given by $0.61\lambda/\mathrm{NA}$, where λ is the wavelength and NA is the numerical aperture. For the configurations corresponding to the three images in Figure 5, the physical resolution limits are $13\,\mu$m, $4.9\,\mu$m, and $2.3\,\mu$m, in a, b, and c, respectively. The smallest resolved element in each case is indicated by an arrow. These elements have 40, 114, and 228 line pairs per mm in a, b, and c, respectively.

A computer with a Pentium III processor with 1.0 GHz clock frequency was used in the reconstruction and the computation time varied from 0.5 s to 20 s depending on the used number of pixels. Images were reconstructed initially with no oversampling to determine the correct object region and to make certain that all parameters had been chosen properly. To get maximum resolution *i.e.*, to reach the physical resolution limit, six oversamplings were made in each dimension which gives a pixel size in the reconstruction plane of $1.13\,\mu$m with the Kodak KAF3200E sensor.

In Figure 6, images are shown with different reconstruction distances. This is done to evaluate the depth resolution of the microscope. The last element in the 7:th series is clearly seen at a distance of 44 mm which gives a maximum resolution of 228 line pairs per mm corresponding to a resolution $4.4\,\mu$m. These images were recorded with a numerical aperture of 0.17. As can be seen in the images the resolution is higher in the horizontal direction than in the vertical direction. It is also observed that the vertical lines and the horizontal lines are in focus at different depths. The better resolution in the horizontal direction can be explained by the rectangular shape of the sensor. It is more difficult to explain the different depth of

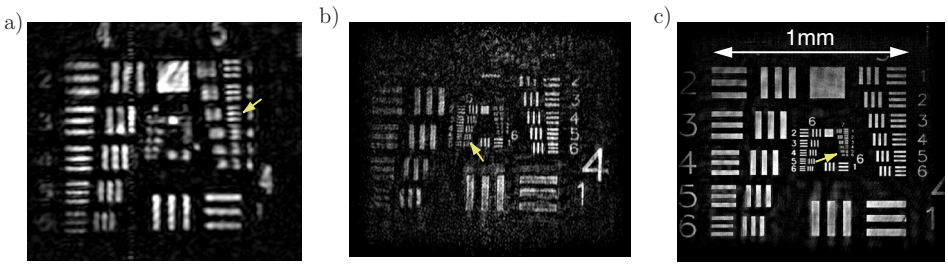

Figure 5: Comparison between the three sensors in Table 1. From left to right: the STMicroelectronics VV5410 sensor at distance 43 mm, the Mintron MTV-1802CB camera at distance 40 mm, and the Kodak KAF3200E sensor at distance 44 mm. The smallest resolved elements are indicated by the arrows. An enlargement of the central part of c) is shown in Figure 6.

focus. One possible explanation is that the GRIN lens is astigmatic [1]. If this is the case, an accurate model of the reference field can be used to solve the problem. A smaller distance than 44 mm between the camera and the object would increase the numerical aperture and accordingly increase the resolution. However, this leads to an under-sampling of the interference pattern and consequently the image quality deteriorate. The sensitivity of the reference position was also tested. The effect from a perturbation of the reference position 50 μm was only a corresponding 50 μm shift of the image.

The Fourier holography setup was also tested for transparent objects. In Figure 7, a reconstructed image of a glass plate with attached 8 μm glass spheres is depicted. The majority of the glass spheres have gathered to form clusters as can be seen in the upper right corner if the image. The lower part of the image shows the edge of the glass plate.

5 Discussion

In this study the Fourier holography setup has been tested. A resolution of 228 line pairs per mm has been experimentally demonstrated. The resolution is shown to be limited by the number of pixels of the sensor and the distance between the reference source and the object (2.1). With the GRIN lens attached to the beam splitter, as described in the setup, the minimum distance between the point source and the object is about 0.5 mm. This was not the case in the reconstructed images in Figure 5 and Figure 6 because of the design of the resolution test target. With other types of objects this distance could be reduced to 0.5 mm which would increase the fringe spacing in the interference patterns. This would make it possible to shorten the object-sensor distance and hence increase the numerical aperture and consequently the resolution (2.1). It is also possible to increase the NA by decreasing the required number of samplings per fringe. This necessitate an accurate modeling of the sensor such that the sensor characteristic can be deconvolved [10]. Here, the simple model of equally sensitive rectangular patches have been tested. However, the deconvolution

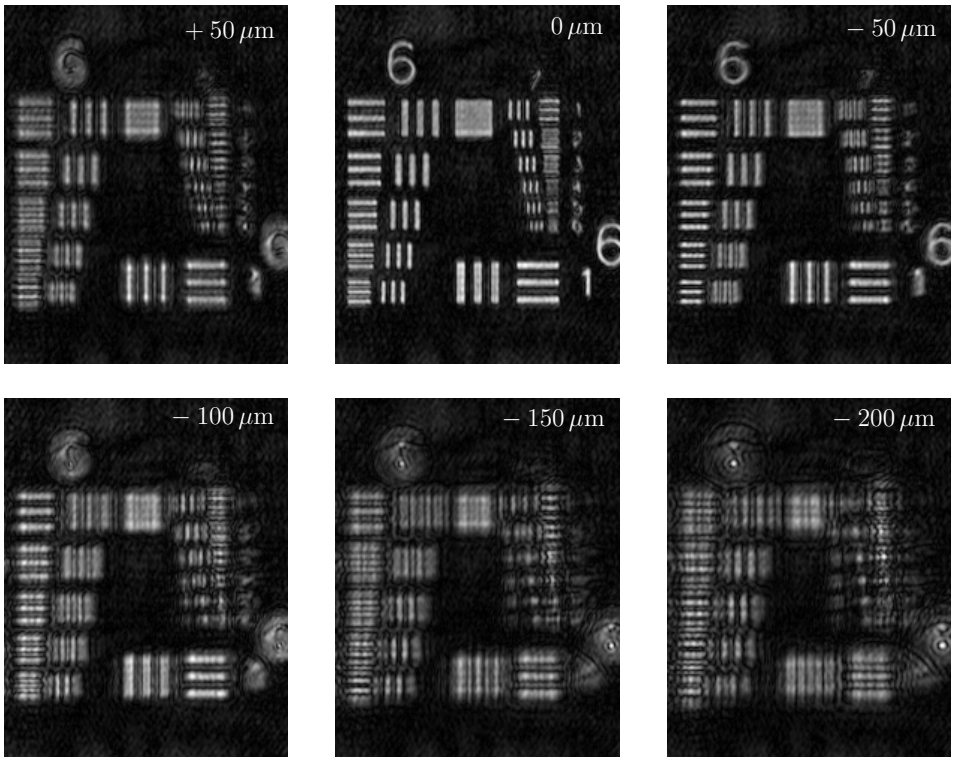

Figure 6: Reconstructions of the USAF test target with the Kodak KAF3200E sensor at the original object sensor distance 44 mm. The reconstructed images are evaluated at the distances $-200\,\mu$m to $50\,\mu$m in step of $50\,\mu$m from the original position. The last element in the 7:th series (228 line pairs per mm) is clearly resolved at the original distance.

did not improve the image quality in this case.

It is also very promising that the image quality is good even though the reference field is modeled as a point source. To improve the image quality even further, it is possible to incorporate a more realistic reference field, *e.g.*, astigmatism [1] effects and the phase error induced by internal reflections in glass plates.

The inversion algorithm is shown to be accurate and relatively fast. However, to reach a real-time image updates, the algorithm has to be accelerated. The most time-consuming part involves calculations of large two-dimensional Fourier transforms. It is possible to improve the performance either by distributing the calculations over an array of computers, or it can be done using a specialized hardware solution [9]. In this project, the latter method will be used to speed up the computations. One obvious reason for this is that FFT calculations are well suited for hardware implementation. Another reason is that dedicated hardware is more cost efficient than using a set of ordinary computers.

The hardware accelerator will at the first stage be implemented on a FPGA development board from AVNET using a Xilinx Virtex-E device. The recorded images will be located in synchronous dynamic memory (SDRAM) to achieve the highest throughput. An early estimation is to be able to calculate about $5 - 10$

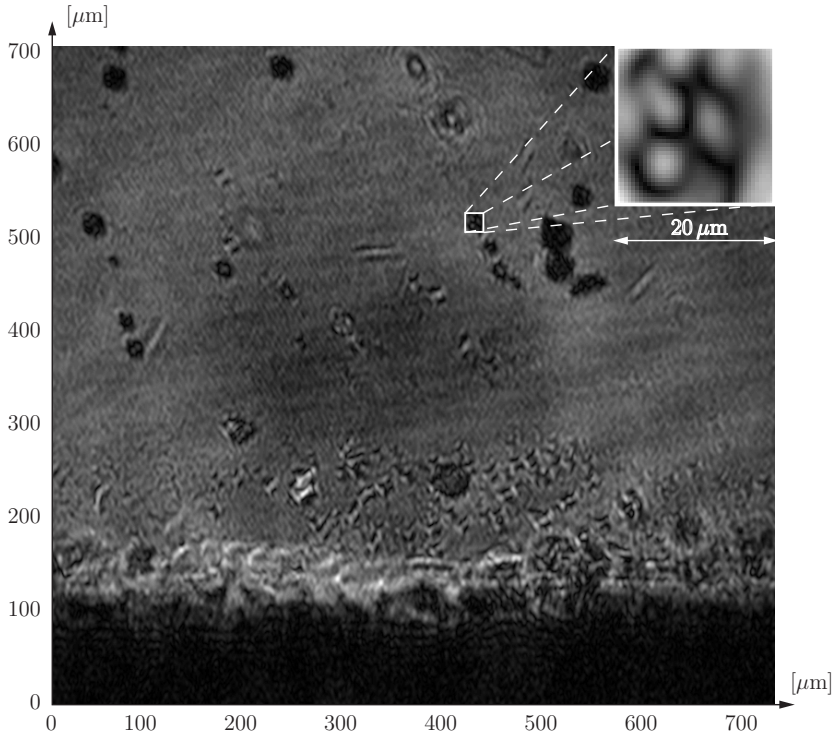

Figure 7: Reconstructed image of a glass plate with attached 8 μm glass spheres. The edge of the glass plate is shown in the lower part of the image.

images per second. The second stage will be to create a System-On-Chip solution including the hardware accelerator and the required memory controllers. The final design will be fabricated in the Alcatel Microelectronics 0.35 μm CMOS technology. Using a System-on-Chip approach, the performance will be further improved.

Acknowledgments

We thank Margaret Cheney, Rensselaer Polytechnic Institute, USA for her interest in the project and for several valuable discussions. We also thank the Department of Physics, Lund University, Sweden for their assistance in the experimental work. This work is funded by the Competence Center for Circuit Design (CCCD), Department of Electroscience, Lund University, Sweden and their support is gratefully acknowledged.

References

[1] J. Atencia and M. Quintanilla. Ray abberration for a biaxial holographic imaging system. *Optics Communications*, **199**, 325–344, December 2001.

[2] M. Born and E. Wolf. *Principles of Optics*. Cambridge University Press, Cambridge, U.K., seventh edition, 1999.

[3] C. Buraga-Lefebvre, S. Coëtmellec, D. Lebrun, and C. Özkul. Application of wavelet transform to hologram analysis: three-dimensional location of particles. *Optics and Lasers in Engineering*, **33**, 409–421, 2000.

[4] H. J. Caulfield. *Handbook of optical holography.* Academic Press, New York, 1979.

[5] T. H. Demetrakopoulos and R. Mittra. Digital and optical reconstruction fo images from suboptical diffraction patterns. *Appl. Opt.*, **13**(3), 665–670, March 1974.

[6] D. Dirksen, H. Droste, B. Kemper, H. Deleré, M. Deiwick, H. H. Scheld, and G. von Bally. Lensless Fourier holography for digital holographic interferometry on biological samples. *Optics and Lasers in Engineering*, **36**, 241–249, 2001.

[7] S. Grilli, P. Ferraro, S. D. Nicola, A. Finizio, G. Pierattini, and R. Meucci. Whole optical wavefields reconstruction by Digital Holography. *Optics Express*, **9**(6), 294–302, September 2001.

[8] W. S. Haddad, D. Cullen, J. C. Solem, J. W. Longworth, A. McPherson, K. Boyer, and C. K. Rhode. Fourier-transform holographic microscope. *Appl. Opt.*, **31**(24), 4973–4978, 1992.

[9] S. He. *Concurrent VLSI Architectures for DFT Computing and Algorithms for Multi-output Logic Decomposition.* PhD thesis, Lund Institute of Technology, Department of Applied Electronics, P.O. Box 118, S-221 00 Lund, Sweden, January 1996. CODEN: LUTEDX/(TETE-1015)/1-159(1995).

[10] P. C. D. Hobbs. *Building Electro-Optical Systems: Making It All Work.* John Wiley & Sons, New York, 2000.

[11] M. Jacquot, P. Sandoz, and G. Tribillon. High resolution digital holography. *Optics Communcations*, **190**, 87–94, 2001.

[12] S. Lai, B. Kemper, and G. von Bally. Off-axis reconstruction of in-line holograms for twin-image elimination. *Optics Communications*, **169**, 37–43, 1999.

[13] E. Leith, J. Upatnieks, and K. A. Haines. Microscopy by wavefront reconstruction. *J. Acoust. Soc. Am.*, **55**(8), 981–986, 1965.

[14] U. Schnars and W. Jüptner. Direct recording of holograms by a CCD target and numerical reconstruction. *Appl. Opt.*, **33**(2), 179–181, 1994.

[15] S. Seebacher, W. Osten, T. Baumbach, and W. Jüptner. The determination of material parameters of microcomponents using digital holography. *Optics and Lasers in Engineering*, **36**, 103–126, 2001.

[16] C. Wagner, S. Seebacher, W. Osten, and W. Jüptner. Digital recording and numerical reconstruction of lensless Fourier holograms in optical metrology. *Appl. Opt.*, **38**(22), 4812–4820, August 1999.

[17] W. Xu, M. H. Jericho, I. A. Meinertzhagen, and H. J. Kreuzer. Digital in-line holography for biological applications. *Cell Biology*, **98**(20), 11301–11305, September 2001.